Supporting Information

Gate-Reconfigurable Metal-Oxide/Polymer Heterojunction Phototransistors for Broadband Photodetection and Multifunctional Opto-Synaptic Computing

Jia Li, Yali Yu, Min Guo, Xiaolong Li, Xinmu Chen, Guozhen Bai, Zhidong Lou, Yanbing Hou, Feng Teng, and Yufeng Hu*

Key Laboratory of Luminescence and Optical Information, Ministry of Education, Institute of Optoelectronic Technology, Beijing Jiaotong University, Beijing, 100044, P.R. China

E-mail: yfhu@bjtu.edu.cn

Keywords: Phototransistor, Organic/inorganic heterojunction, Positive/negative photoconductance, Synaptic plasticity

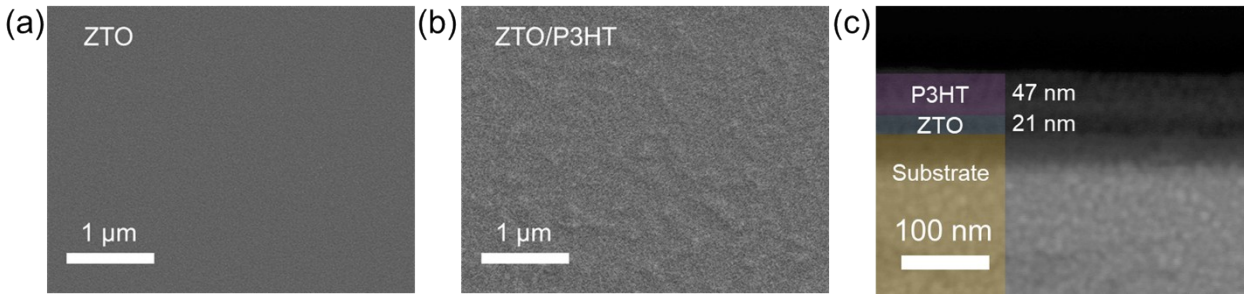

Figure S1. SEM images of the solution-processed (a) ZTO and (b) P3HT film on it. (c) Cross-sectional SEM image of the device.

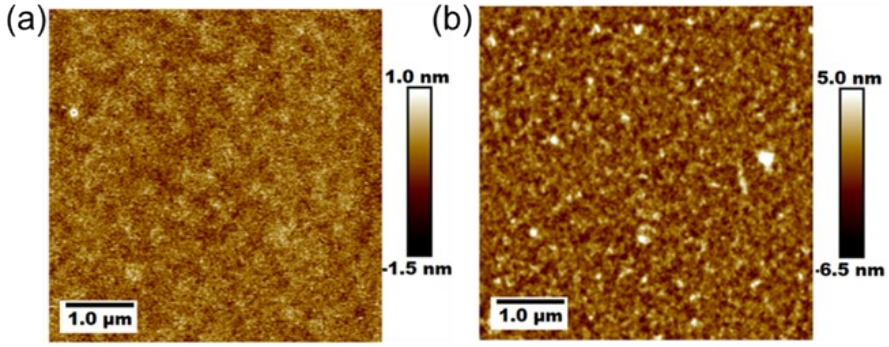

Figure S2. AFM image of (a) ZTO and (b) P3HT deposited on it.

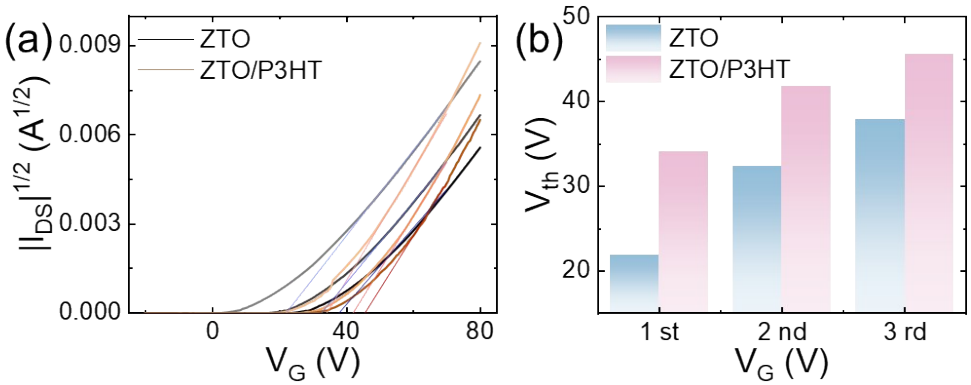

Figure S3. (a) The $|I_{DS}|^{1/2}$-V_G curves for single-layer and double-layer devices, along with the comparison of the derived (b) threshold voltages.

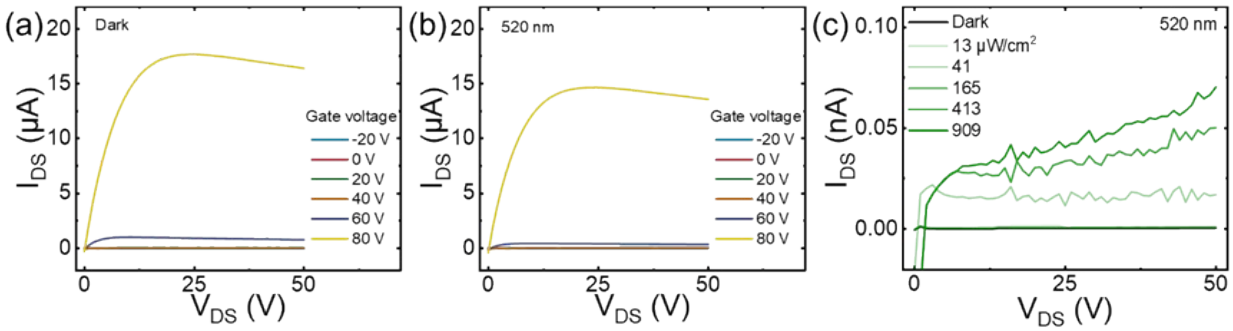

Figure S4. Output curves of the device under (a) dark, (b) 520 nm (13 μW/cm²) illumination. (c) Output curves with varying light intensities at 520 nm (V_G=0 V).

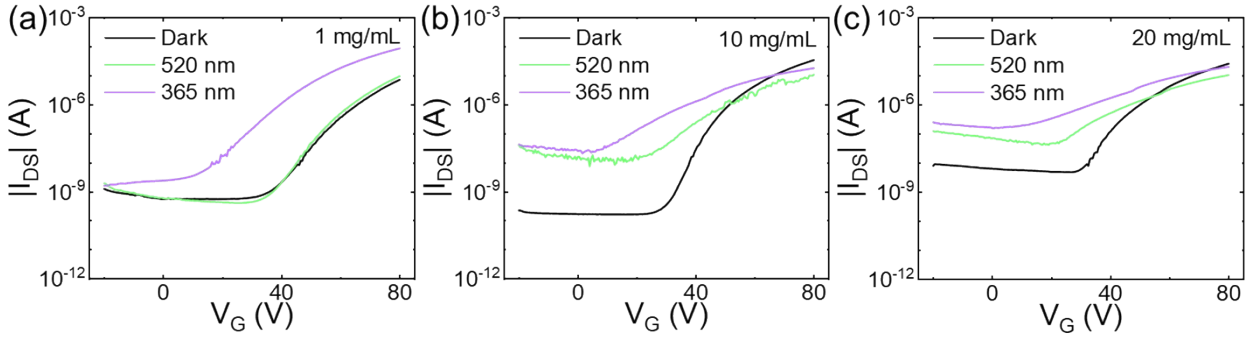

Figure S5. Transfer curves of devices fabricated using P3HT solutions with concentrations of (a)1 mg/mL, (b)10 mg/mL, and (c) 20 mg/mL.

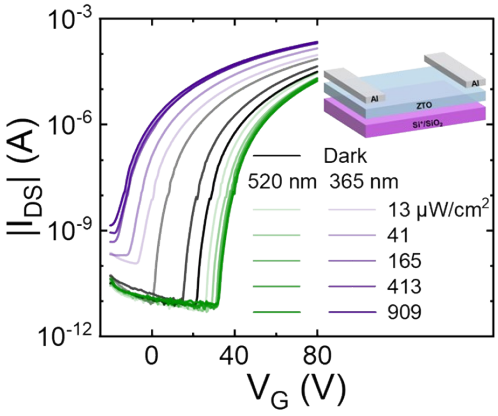

Figure S6. Transfer curves of the single-layer device under illumination at multiple wavelengths and intensities.

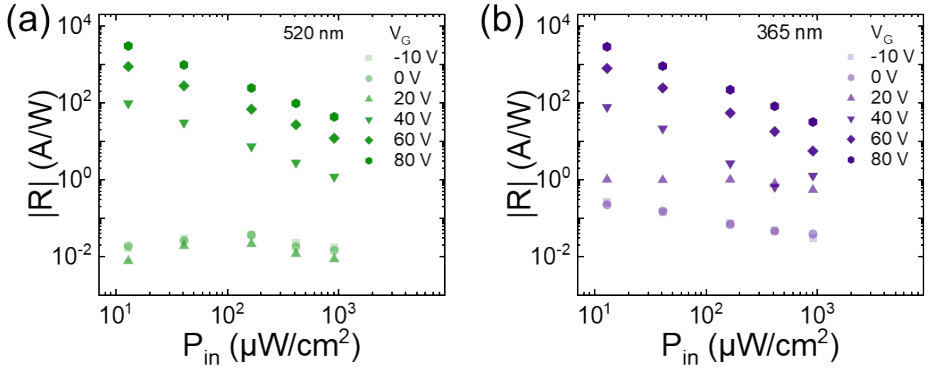

Figure S7. R as a function of P_{in} and V_G under (a) 520 nm and (b) 365 nm illumination.

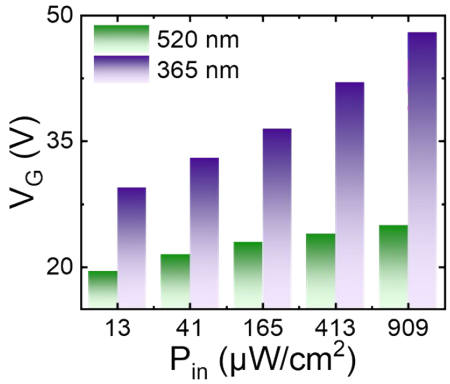

Figure S8. V_G corresponding to the transition between PPC and NPC in the bilayer device

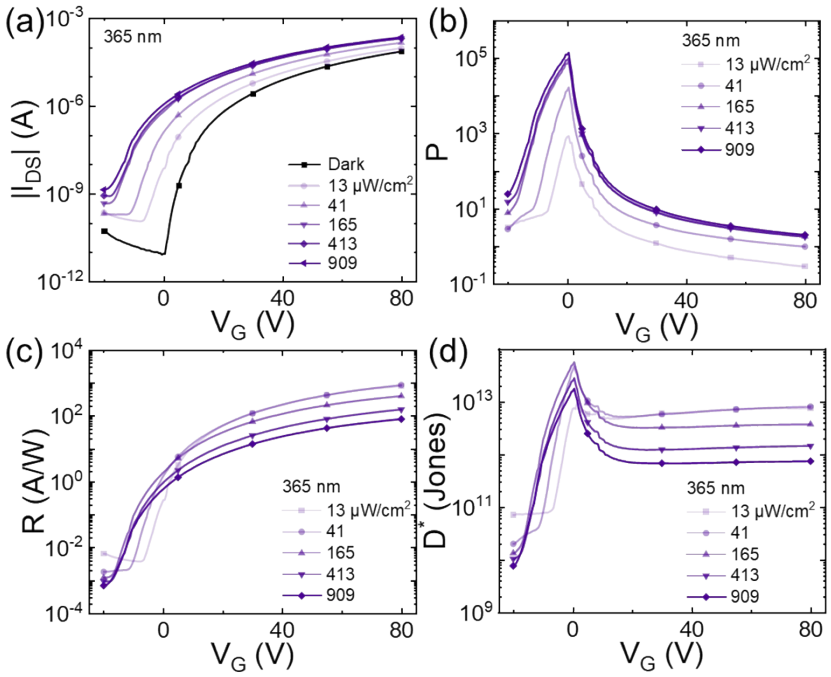

Figure S9. (a) Comparison of transfer curves, (b) P, (c) R, and (d) D^* of the single-layer ZTO device under 365 nm illumination.

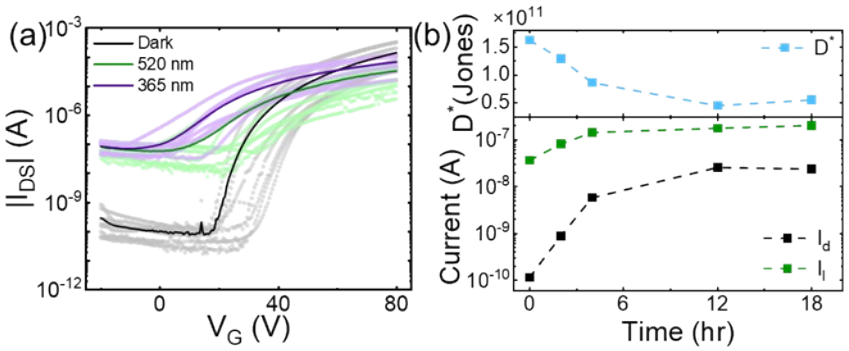

Figure S10. (a) Device reproducibility and (b) stability in the atmospheric environment (V_G=-10 V, V_{DS}=50 V, 520 nm, light intensity is 413 μW/cm^2).

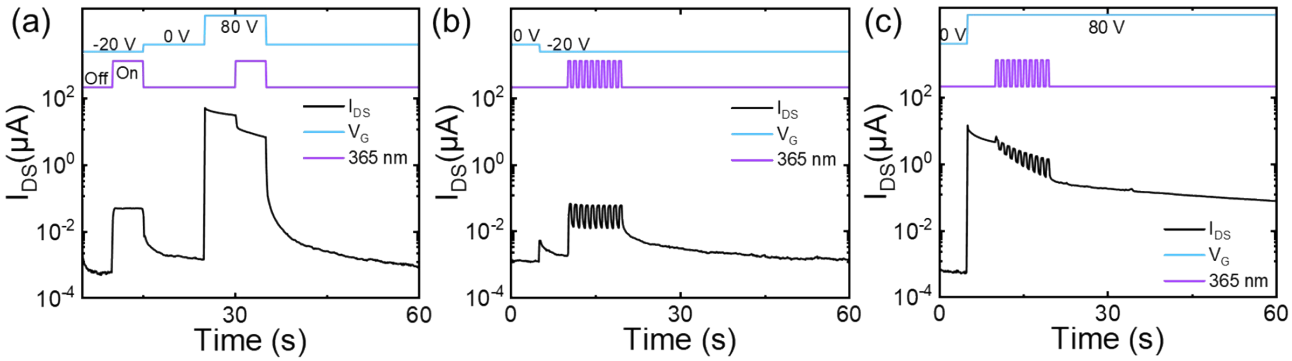

Figure S11. (a) Modulation of I_{DS} by 365 nm illumination under different V_G. Photocurrent response to ten constant optical pulses (1 Hz) under (b) off-state and (c) on-state.

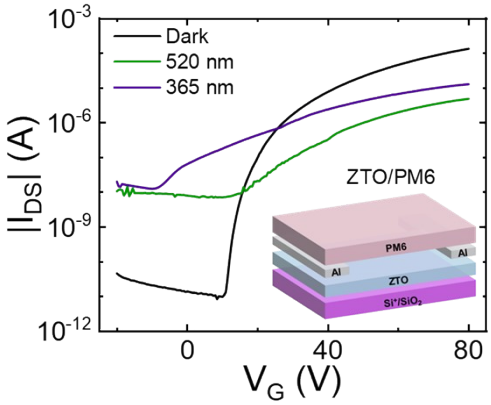

Figure S12. PPC and NPC responses of the Si$^+$/SiO$_2$/ZTO/Al–Al/PM6 device under 520 nm and 365 nm illumination.

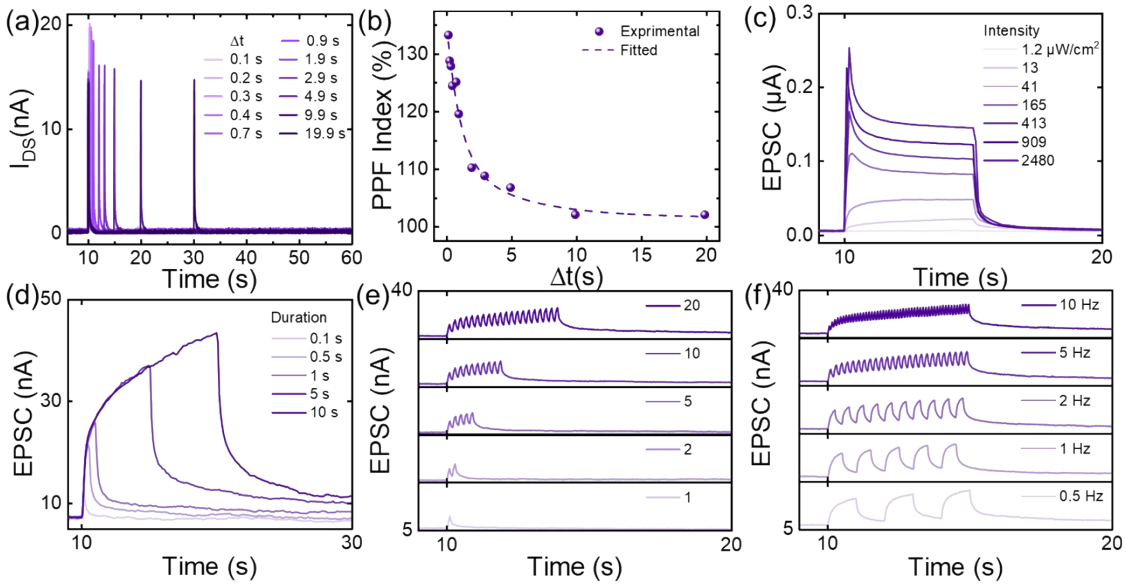

Figure S13. Synaptic response behavior of the device under 365 nm illumination. (a) Paired-pulse facilitation (PPF) behavior. (b) Dependence of PPF index on Δ*t*. (c) SIDP, (d) SDDP, (e) SNDP and (f) SRDP.

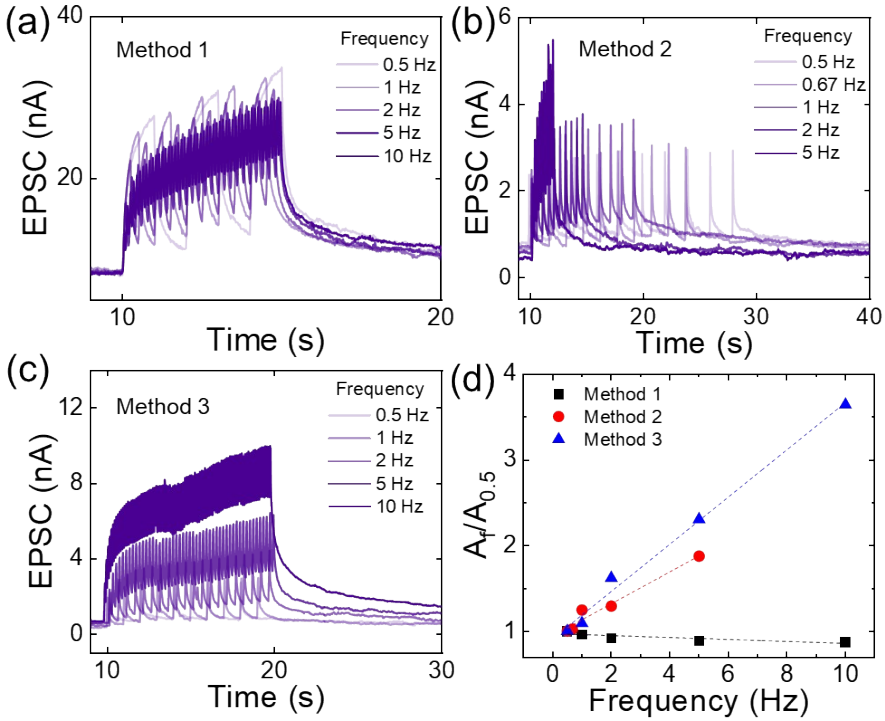

Figure S14. Influence of frequency modulation on EPSC under (a) Method 1, (b) Method 2 and (c) Method 3 with 365 nm illumination. (d) The corresponding $A_f/A_{0.5}$–f curve.

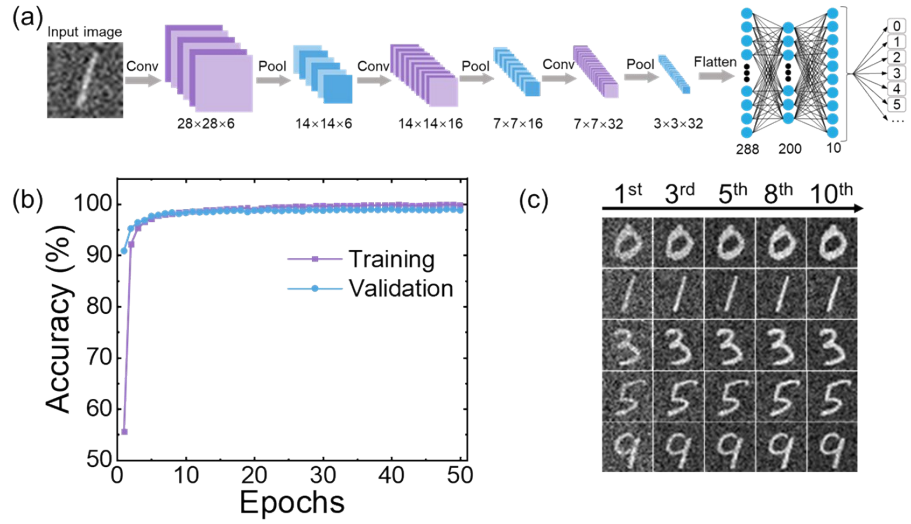

Figure S15. (a) Schematic illustration of the CNN architecture used in this work, consisting of three convolutional layers alternately connected with pooling layers, followed by a flatten layer and a fully connected layer for final classification of handwritten digits (0–9). The CNN is implemented entirely in software and serves solely as an algorithmic evaluation tool. (b) The accuracy curves for training (60,000 images) and validation (10,000 images) based on the MNIST handwritten dataset demonstrate the stable convergence characteristics and excellent generalization performance of the CNN model. (c) Representative examples of virtual input images generated under different effective light response conditions, using the original MNIST pixel grayscale values as incident light intensity. Simulations were performed by adjusting the number of light pulses based on device characteristics extracted from experiments. An increase in pulse count corresponds to enhanced image contrast and reduced noise levels. All datasets used in this figure are generated by incorporating experimentally extracted parameters from a single device, including photoresponse amplitude and noise characteristics. No physical implementation of the CNN or device array integration is involved.